



# ETHOS – an Effective Theory of Structure Formation: detecting dark matter interactions through the Lyman- $\alpha$ forest

Sownak Bose<sup>1,1</sup>★ Mark Vogelsberger,<sup>2</sup>★ Jesús Zavala,<sup>3</sup> Christoph Pfrommer,<sup>4</sup>  
Francis-Yan Cyr-Racine,<sup>5,6</sup> Sebastian Bohr<sup>3</sup> and Torsten Bringmann<sup>7</sup>

<sup>1</sup>*Harvard-Smithsonian Center for Astrophysics, 60 Garden Street, Cambridge, MA 02138, USA*

<sup>2</sup>*Department of Physics, Kavli Institute for Astrophysics and Space Research, Massachusetts Institute of Technology, Cambridge, MA 02139, USA*

<sup>3</sup>*Center for Astrophysics and Cosmology, Science Institute, University of Iceland, Dunhagi 5, 107 Reykjavik, Iceland*

<sup>4</sup>*Leibniz-Institut für Astrophysik Potsdam, An der Sternwarte 16, D-14482 Potsdam, Germany*

<sup>5</sup>*Department of Physics, Harvard University, Cambridge, MA 02138, USA*

<sup>6</sup>*Department of Physics and Astronomy, University of New Mexico, Albuquerque, NM 87131, USA*

<sup>7</sup>*Department of Physics, University of Oslo, Box 1048, N-0371 Oslo, Norway*

Accepted 2019 May 6. Received 2019 April 28; in original form 2018 November 27

## ABSTRACT

We perform a series of cosmological hydrodynamic simulations to investigate the effects of non-gravitational dark matter (DM) interactions on the intergalactic medium (IGM). In particular, we use the ETHOS framework to compare statistics of the Lyman- $\alpha$  forest in cold dark matter (CDM) with an alternative model in which the DM couples strongly with a relativistic species in the early universe. These models are characterized by a cut-off in the linear power spectrum, followed by a series of ‘dark acoustic oscillations’ (DAOs) on sub-dwarf scales. While the primordial cut-off delays the formation of the first galaxies, structure builds up more rapidly in the interacting DM model compared to CDM. We show that although DAOs are quickly washed away in the non-linear clustering of DM at  $z \lesssim 10$ , their signature can be imprinted prominently in the Lyman- $\alpha$  flux power spectrum at  $z > 5$ . On scales larger than the cut-off ( $k \sim 0.08 \text{ s km}^{-1}$  for the specific model considered here), the relative difference to CDM is reminiscent of a warm dark matter (WDM) model with a similar initial cut-off; however, the redshift evolution on smaller scales is distinctly different. The appearance and disappearance of DAOs in the Lyman- $\alpha$  flux spectrum provides a powerful way to distinguish interacting DM models from WDM and, indeed, variations in the thermal history of the IGM that may also induce a small-scale cut-off.

**Key words:** methods: numerical – intergalactic medium – dark matter.

## 1 INTRODUCTION

In the standard picture of structure formation, the enigmatic dark matter (DM) particle is assumed to be a kinematically cold, collisionless, and non-baryonic entity. This ‘cold’ dark matter (CDM) model has predictive power, a feature that has been exploited over the past four decades in a rigorous campaign of numerical simulations that has established CDM as part of the standard cosmological paradigm. The great success of this model lies in the finding that the same theory that accounts for the temperature anisotropies in the cosmic microwave background at early times (Spergel et al. 2003; Planck Collaboration XIII 2016) has been similarly successful at reproducing the large-scale clustering of

galaxies at present day (Colless et al. 2001; Cole et al. 2005; Eisenstein et al. 2005; Zehavi et al. 2011).

At the regime of dwarf galaxies, however, a number of ‘small-scale challenges’ have been claimed to afflict the CDM paradigm. Chief amongst them are the so-called missing satellites (e.g. Klypin et al. 1999; Moore et al. 1999), too big to fail (Boylan-Kolchin, Bullock & Kaplinghat 2011), cusp–core (e.g. Flores & Primack 1994; de Blok et al. 2001), and plane of satellites problems (e.g. Ibata et al. 2014; Pawlowski et al. 2014). For a thorough overview of this subject, we refer the reader to the recent review by Bullock & Boylan-Kolchin (2017). While these issues have been used to motivate DM candidates beyond CDM, it should be cautioned that the small-scale problems are only firmly established with simulations that include the modelling of the CDM component only. These issues may in fact be resolved within the CDM paradigm once the impact of gas and stellar physics is better understood and fully taken into account. This has been permitted by the increasing

\* E-mail: [sownak.bose@cfa.harvard.edu](mailto:sownak.bose@cfa.harvard.edu) (SB); [mvogelsb@mit.edu](mailto:mvogelsb@mit.edu) (MV)

sophistication of hydrodynamical simulations (e.g. Dubois et al. 2014; Vogelsberger et al. 2014a,c; Schaye et al. 2015; Springel et al. 2018), which self-consistently track the co-evolution of dark and baryonic matter. Although hydrodynamical simulations differ in detail, they have shown universally that the interaction between DM and baryons through processes associated with galaxy formation – such as gas cooling, photoionization, and feedback – change both the census of the galactic population (e.g. Kauffmann, White & Guiderdoni 1993; Kim, Peter & Hargis 2017; Read et al. 2017) and the internal structure of DM haloes (e.g. Di Cintio et al. 2014; Pontzen & Governato 2014; Sawala et al. 2016; Fitts et al. 2017) relative to simulations modelling only the DM component.

In fact, perhaps the greatest challenge to the CDM model, at least in terms of its appeal as a complete structure formation theory, is that despite intense efforts at discovering CDM-like particles, the search has been fruitless so far. Most of these efforts have focused on weakly interacting massive particles (WIMPs), which are one of the best-motivated CDM candidates in great part due to their potential connection with supersymmetry (Jungman, Kamionkowski & Griest 1996). After the successful discovery of the Higgs boson, it was hoped that the Large Hadron Collider (LHC) would find evidence for supersymmetry, giving credence to WIMPs and the CDM model, but thus far the LHC has failed to provide any evidence of this kind. WIMPs have also remained elusive to both direct (Aprile et al. 2018) and indirect detection (e.g. Albert et al. 2017) experiments. Furthermore, promising observational anomalies that might be connected to DM either have disappeared or are explained with non-DM astrophysical sources; for example, the excess of gamma-rays at the Galactic Centre, which has been ascribed to the self-annihilation of WIMPs (e.g. Hooper & Goodenough 2011; Daylan et al. 2016), may instead be explained by a population of unresolved millisecond pulsars (e.g. Bartels, Krishnamurthy & Weniger 2016; Lee et al. 2016; Fermi-LAT Collaboration 2017), or an overdensity of stars in the Galactic bulge (Macias et al. 2018).

As long as DM remains undetected in the laboratory, it is worth considering well-motivated alternatives to CDM and their implications for structure formation. A popular alternative is *warm* dark matter (WDM; Bond & Szalay 1983; Colín, Avila-Reese & Valenzuela 2000; Bode, Ostriker & Turok 2001), in which the DM particles have a non-negligible velocity dispersion in the early universe. The resulting free-streaming of these particles suppresses density fluctuations below a characteristic scale determined by the rest mass of the particles and their thermal history; this delays the formation of the first structures and reduces the abundance of low-mass galaxies in the process (e.g. Zavala et al. 2009; Macciò & Fontanot 2010; Lovell et al. 2012; Schneider et al. 2012; Kennedy et al. 2014; Bose et al. 2016a; Bozek et al. 2019). In the linear regime, the free-streaming of WDM particles is manifested as a nearly exponential cut-off in the linear power spectrum relative to CDM. In other well-motivated DM models, there may exist a coupling between the DM and a relativistic species (e.g. neutrinos or ‘dark’ radiation) in the early universe. In these so-called interacting dark matter (iDM) models, the ensuing radiation pressure inhibits the growth of small-scale fluctuations and also results in a (collisional) cut-off in the linear power spectrum, but with a more complex behaviour than in WDM, exhibiting dark acoustic oscillations (e.g. Carlson, Machacek & Hall 1992; Boehm et al. 2002; Ackerman et al. 2009; Cyr-Racine & Sigurdson 2013; Buckley et al. 2014; Boehm et al. 2014; Bringmann et al. 2016). Another promising alternative is offered by self-interacting dark matter (SIDM) models, in which multiple scattering events between DM particles can significantly

change the internal structure of DM haloes compared to CDM in the non-linear regime (e.g. Spergel & Steinhardt 2000; Yoshida et al. 2000; Davé et al. 2001; Colín et al. 2002; Vogelsberger, Zavala & Loeb 2012; Rocha et al. 2013; Zavala, Vogelsberger & Walker 2013; Vogelsberger et al. 2014b; Elbert et al. 2015; Kaplinghat, Tulin & Yu 2016; Robertson et al. 2018; Vogelsberger et al. 2018).

While these different DM species come from a diverse range of particle physics models with vastly different production mechanisms, the resulting effect on structure formation is similar in many cases. This is particularly evident in the case of WDM and iDM, both of which suppress small-scale structure by inducing a cut-off in the linear power spectrum. In this work, we consider examples of these models within the generalized framework of structure formation ETHOS (Cyr-Racine et al. 2016; Vogelsberger et al. 2016), which addresses such degeneracies by providing a mapping between parameters associated with DM physics and parameters relevant for structure formation. The flexibility afforded by this formalism potentially allows the investigation of a general class of model parameters (cut-off scale, self-interaction cross-section, DM–radiation coupling, etc.) and their impact on the formation of galaxies without needing to simulate every point in the allowed parameter space. Previous analyses connected to this programme have focused on the predictions of these models for the internal content of DM haloes (Vogelsberger et al. 2016; Brinckmann et al. 2018; Sameie et al. 2018; Sokolenko et al. 2018), the diverse rotation curves of dwarf galaxies (Creasey et al. 2017), the tidal stripping of satellites in the Galactic halo (Dooley et al. 2016), and the possibility of detecting these DM candidates through gravitational lensing (Díaz Rivero et al. 2018). Finally, the most recent investigation has considered the high-redshift galaxy population and reionization history in this general class of models (Das et al. 2018; Lovell et al. 2018). In this paper, we are particularly interested in the signatures of new DM phenomenology (see Section 2 for details) that may be imprinted in statistics of the Lyman- $\alpha$  forest.

The Lyman- $\alpha$  forest has proven to be a remarkably powerful probe of the nature of DM in the mildly non-linear regime. Measurements of the flux spectrum using observed quasar (QSO) sightlines have been used repeatedly to infer the clustering of matter on these scales (e.g. Croft et al. 1998, 1999; McDonald et al. 2000; Palanque-Delabrouille et al. 2013). The flux spectrum is a particularly powerful probe of processes relating to early galaxy formation and the small-scale behaviour of DM particles by providing an insight on the matter power spectrum at relatively high redshift. In fact, it is now well established that the *observed* flux spectrum displays a cut-off in power on scales smaller than  $k \sim 0.03 \text{ s km}^{-1}$ , a feature that has been used to constrain the free-streaming properties of DM particles (e.g. Viel et al. 2005; Seljak et al. 2006; Viel et al. 2013; Baur et al. 2016; Kobayashi et al. 2017; Iršič et al. 2017a; Garzilli et al. 2018; Murgia, Iršič & Viel 2018; Nori et al. 2018).

A cut-off in the flux spectrum towards small scales may, however, originate from purely baryonic processes (e.g. Zaldarriaga, Hui & Tegmark 2001; Peebles et al. 2010; Rorai, Hennawi & White 2013; Nasir, Bolton & Becker 2016). The first effect, known as Jeans smoothing, is a result of increased gas pressure in the intergalactic medium (IGM) due to boosted temperatures induced by the onset of reionization. The degree of Jeans smoothing depends on both the integrated heat injection and exact timing of reionization (e.g. Gnedin & Hui 1998; Kulkarni et al. 2015; Oñorbe et al. 2017). A second effect is brought upon by random thermal motions of

the gas, resulting in Doppler broadening of Lyman- $\alpha$  forest lines, further smoothing small-scale power in the flux spectrum. The degenerate behaviour of the thermal history of the IGM and the free-streaming properties of DM make it difficult to pinpoint the physical interpretation of the observed cut-off in the flux spectrum and may indeed relax current constraints on the rest mass of the WDM particle (Garzilli, Boyarsky & Ruchayskiy 2017). Never the less, it is clear that the Lyman- $\alpha$  forest provides a unique probe into mildly non-linear scales at high redshift, which is the regime where most alternative DM models exhibit the strongest deviations from CDM. The main goal of this paper is to show that, if strong enough, non-gravitational features (dark acoustic oscillations) in the primordial power spectrum of iDM models can remain imprinted in the Lyman- $\alpha$  flux spectrum.

The layout of this paper is as follows. In Section 2, we briefly describe the DM particle physics model considered in this work, highlighting its connection to the general ETHOS framework. Section 3 describes the numerical set-up used for this investigation, detailing our simulations and the analysis pipeline used to extract mock Lyman- $\alpha$  absorption spectra from them. Section 4 presents our main findings. Finally, our conclusions are summarized in Section 5.

## 2 DARK MATTER MODEL

In this work, we study structure formation in DM theories in which early-universe interactions with a relativistic species (see e.g. Carlson et al. 1992; Böhm et al. 2002; Ackerman et al. 2009; Feng et al. 2009; van den Aarssen, Bringmann & Pfrommer 2012; Chu & Dasgupta 2014; Buen-Abad, Marques-Tavares & Schmaltz 2015; Bringmann et al. 2016; Chacko et al. 2016) lead to a modified initial spectrum of density fluctuations as compared to standard CDM. The general phenomenology of such models is described in detail in Cyr-Racine et al. (2016) within the ETHOS framework, while the nonlinear evolution of structure within these models was studied in Buckley et al. (2014) and Vogelsberger et al. (2016; see also Böhm et al. 2014; Schewtschenko et al. 2015). In these theories, the DM forms a fluid that is tightly coupled to a relativistic species (e.g. neutrinos or dark radiation) at early times, much like the standard baryon-photon plasma before the epoch of recombination. Within this ‘dark’ fluid, the large radiation pressure prohibits the growth of DM fluctuations and allows the propagation of acoustic waves to large cosmological distances (Cyr-Racine et al. 2014). Just like the more well-known baryon acoustic oscillations (BAOs), these *dark acoustic oscillations* (DAOs) become imprinted on the spectrum of matter fluctuations at late times, providing us with a potential smoking gun for physical processes taking place in the early Universe. Due to the finite value of the coupling between DM and the relativistic species, the DAOs are usually damped on scales smaller than the radiation mean free path, in a process similar to standard Silk damping (Silk 1968).

The resulting shape of the linear matter power spectrum is largely determined by how quickly the DM kinetically decouples from the radiation bath. Quantitatively, near the redshift of DM kinetic decoupling,  $z_D$ , we have approximately

$$(\dot{\kappa}_\chi/\mathcal{H})|_{z \sim z_D} \simeq (z/z_D)^n, \quad (1)$$

where  $\dot{\kappa}_\chi$  is the ‘drag opacity’ or interaction rate between DM and the relativistic species, and  $\mathcal{H}$  is the conformal Hubble expansion rate. Note that  $\dot{\kappa}$  denotes a derivative with respect to conformal time.

In general, a larger value for the power-law index,<sup>1</sup>  $n$ , results in a greater number of undamped DAOs on the small-scale linear power spectrum. Once the non-linear evolution of density fluctuations is taken into account, models with low values of  $n \lesssim 4$  exhibit structure formation that is reminiscent of standard WDM models (Vogelsberger et al. 2016; Murgia et al. 2017). On the other hand, models characterized by a large value of the power-law index  $n \gtrsim 6$  (which we hereafter refer to as ‘strong’ DAO models, sDAO) have a structure formation history that is appreciably different from WDM, as first discussed in Buckley et al. (2014). We note that the models used in Vogelsberger et al. (2016), Lovell et al. (2018), and Das et al. (2018) all have  $n = 4$ , and thus fall in the former category.

Since our aim is to study Lyman- $\alpha$  constraints on DM theories that have a structure formation history that is distinct from WDM, the present investigation focuses on sDAO models. In particular, we consider an atomic DM (Kaplan et al. 2010, 2011; Cyr-Racine & Sigurdson 2013) in which DM is composed of two massive fermions that are oppositely charged under a new unbroken  $U(1)$  dark gauge force. In this paradigm, the dark sector forms an ionized plasma at early times, until the temperature falls below the binding energy between the two oppositely charged particles, at which point neutral dark atoms form in a process reminiscent to cosmological hydrogen recombination. If this ‘dark’ recombination occurs in or near thermal equilibrium, an extremely rapid kinematic decoupling epoch ensues due to the nearly exponential (Saha-like) nature of bound state formation in this case. This ensures that the power-law index appearing in equation (1) is large ( $n = 6$  for our sDAO model), resulting in a linear matter power spectrum composed of a significant number of undamped DAOs on small scales.

We choose parameters of this model such that the linear matter power spectrum of our sDAO model starts deviating from its CDM counterpart near a comoving wavenumber of  $k \sim 10 h \text{ Mpc}^{-1}$ , which is the scale where current observations of the Lyman- $\alpha$  spectrum become a powerful tool to discriminate different DM models. In the nomenclature of the ETHOS framework, the sDAO model is defined by

$$\{n, a_n, \omega_{\text{DR}}, \alpha_2, \alpha_{l \geq 2}\} = \{6, 6 \times 10^8 \text{ Mpc}^{-1}, 1.25 \times 10^{-8}, 9/10, 1\}$$

while the ETHOS-4 model<sup>2</sup> is defined by

$$\{n, a_n, \omega_{\text{DR}}, \alpha_{l \geq 2}\} = \{4, 414 \text{ Mpc}^{-1}, 1.35 \times 10^{-6}, 3/2\}$$

where  $n$  is the power-law index defined in equation (1),  $a_n$  is the normalization of the drag opacity at redshift  $z_D = 10^7$ ,  $\omega_{\text{DR}} \equiv \Omega_{\text{DR}} h^2$  is the physical energy density in the dark radiation component in units of the critical density and  $\alpha_l$  is a set of coefficients that defines the angular dependence of the DM–dark radiation scattering cross-section. We refer the reader to section II of Cyr-Racine et al. (2016) for further details. The actual particle physics (i.e. Lagrangian) parameters of the sDAO model are listed in Appendix B.

Fig. 1 illustrates the power spectrum appropriate to this model. For comparison, we also display the matter power spectra for CDM, ETHOS-4, as well as WDM thermal relics with mass 1.6 and 3.3 keV. The parameters for ETHOS-4 were especially selected to alleviate the missing satellites, too big to fail, and core–cusp ‘problems’ in CDM (Section 1) through DM physics alone (Vogelsberger et al.

<sup>1</sup>We note that this power-law index is the same as that used to classify DM models within the ETHOS framework (Cyr-Racine et al. 2016).

<sup>2</sup>We note that the  $a_4$  amplitudes given in Vogelsberger et al. (2016) should be divided by  $h$  to yield the correct values.

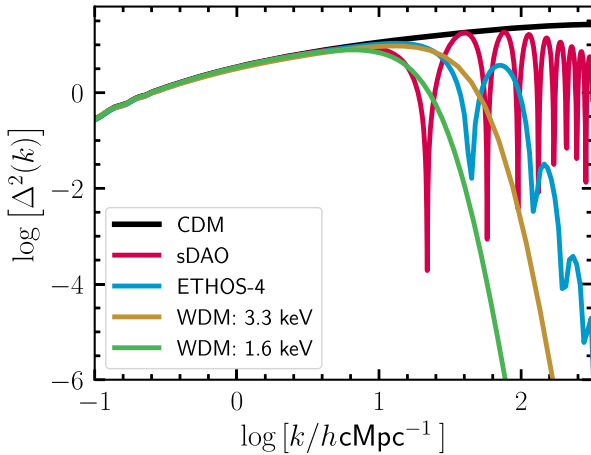


**Figure 1.** Dimensionless power spectra  $[\Delta^2(k) = k^3 P(k)]$  for the CDM (black) and sDAO (red) models used in this work. For comparison, we also show the power spectra for the less extreme ETHOS-4 model (blue; see Vogelsberger et al. 2016), which exhibits a deviation from CDM at a scale comparable to that of a 3.3 keV thermal relic WDM particle (in yellow). On the other hand, the cut-off scale for the sDAO model is closer to that of a 1.6 keV thermal relic (green). Furthermore, the amplitude of the dark acoustic oscillations (DAOs) in the sDAO model is considerably larger than in ETHOS-4.

2016). Unlike WDM, in which the cut-off continues indefinitely, the ETHOS models show a resurgence of power on smaller scales due to the aforementioned DAOs. Note that because of these DAOs, ETHOS models, in particular sDAO models, have increased small-scale power compared to WDM models with a cut-off at the same scale. We note that the sDAO model, which is our main focus in this paper, may already be strongly constrained by present observations. Our goal here is to investigate if small-scale DAOs may be at all detectable in the Lyman- $\alpha$  forest, rather than to construct a model that matches the data. For this reason, we opt to simulate an iDM scenario that maximizes differences relative to CDM on scales large enough that they may be captured at moderate numerical expense.

### 3 NUMERICAL SET-UP

#### 3.1 Simulations and initial conditions

The simulations we present in this work make use of the cosmological simulation code AREPO (Springel 2010). AREPO employs a hybrid tree/particle-mesh scheme to solve for gravitational interactions of DM particles, and a moving, unstructured Voronoi mesh to solve equations of hydrodynamics. The moving mesh is adaptive in nature, resolving fluids in regions of high density with many more cells of a smaller size than in low-density environments. AREPO has been augmented with a comprehensive model for galaxy formation (Weinberger et al. 2017; Pillepich et al. 2018a), which we use here. In addition, Vogelsberger et al. (2016) present an updated version of AREPO that, in addition to the galaxy formation models mentioned above, also incorporates elastic, isotropic self-interactions of DM particles, while allowing for arbitrary velocity-dependent interaction cross-sections (using an algorithm adapted from the original described in detail in Vogelsberger et al. 2012). While the self-scatterings of DM particles have a pronounced impact on the internal structure of haloes at late times, their influence on the IGM at high redshifts will be sub-dominant to that induced by

the cut-off in the power spectrum; we have therefore turned off self-interactions in the simulations.

Our high-resolution simulations follow the evolution of  $2 \times 512^3$  DM and gas particles from  $z = 127$  to  $z = 0$  in a periodic box of (comoving) size  $29.6 \text{ cMpc}$  ( $20 h^{-1} \text{ cMpc}$ ), resulting in an effective DM particle mass of  $6.41 \times 10^6 M_\odot$ . An individual gas cell has a target mass of  $1.01 \times 10^6 M_\odot$ . This target gas mass also corresponds to the typical mass of a stellar macroparticle representing a stellar population. We enforce that the mass of all cells is within a factor of 2 of the target mass by explicitly refining and de-refining the mesh cells. The comoving softening length for DM particles is set to 1.19 kpc, while the (adaptive) softening applied to a gas cell is set to a comoving minimum value of 185 pc. To check for convergence, we also run a second set of simulations a factor of 2 lower in resolution.

We use the fiducial IllustrisTNG galaxy formation model (Weinberger et al. 2017; Pillepich et al. 2018a) with one change. Namely, we have turned off the magnetohydrodynamics solver as it is not relevant for the analysis presented here. As in the fiducial TNG model, each of our simulations is set up with a time-dependent, spatially uniform ionizing background as described in the model by Faucher-Giguère et al. (2009). The TNG model is built upon the original Illustris galaxy formation model described in Vogelsberger et al. (2013).

Initial conditions for all simulations were generated using the MUSIC code (Hahn & Abel 2011), assuming cosmological parameters derived from Planck Collaboration XIII (2016):  $\Omega_0 = 0.311$  (total matter density),  $\Omega_b = 0.049$  (baryon density),  $\Omega_\Lambda = 0.689$  (dark energy density),  $H_0 = 67.5 \text{ km s}^{-1} \text{ Mpc}^{-1}$  (Hubble parameter), and  $\sigma_8 = 0.815$  (linear rms density fluctuation in a sphere of radius  $8 h^{-1} \text{ Mpc}$  at  $z = 0$ ). The dimensionless linear power spectra used to generate initial conditions are shown in Fig. 1. While the CDM power spectrum exhibits power on all scales, the two ETHOS models cut off at  $\log [k/h \text{ cMpc}^{-1}] \approx 1$ . In this paper we will be concerned with the sDAO model, in which the model parameters have been adjusted to amplify the effect of DAOs, as explained in the previous section. Our goal is to investigate the extent to which the characteristics of DAOs in the ETHOS models can be probed using the Lyman- $\alpha$  forest. To put our results in context, we have also run simulations of the ETHOS-4 and 1.6 keV WDM models at our default resolution. The choice of a 1.6 keV thermal relic is motivated by the fact that the free-streaming scale in this model is identical to the cut-off in sDAO; this helps disentangle small-scale differences induced by the acoustic oscillations from those that are caused by a primordial cut-off. The simulations are analysed to perform mock Lyman- $\alpha$  observations using the procedure that we describe in the following subsection. Finally, we note that simulations that resolve the primordial power-spectrum cut-off are plagued by artificial fragmentation of filaments that condense into ‘spurious’ haloes (e.g. Wang & White 2007; Lovell et al. 2014). These objects are seeded by discreteness of the particle set rather than a true gravitational instability, and must hence be excluded from the analysis. This is a well-known problem in WDM simulations, but is less severe in the ETHOS models that have added small-scale power in the form of DAOs (Buckley et al. 2014; see also Fig. A1). This is especially true at high redshift, which is the regime of interest in this paper. As such, we do not perform any extra steps to classify these objects in the simulations we have run.

#### 3.2 Creating Lyman- $\alpha$ mock absorption spectra

From the outputs of each simulation, we generate synthetic absorption spectra using the methodology outlined in Altay & Theuns

(2013). In short, at each output time, we select 1024 randomly selected skewers<sup>3</sup> oriented parallel to a coordinate axis of the box. Gas cell properties are interpolated on to locations along each skewer using a smoothing kernel; we follow Altay & Theuns (2013) and employ a truncated Gaussian kernel,  $G_t(r, \sigma)$ , which is defined as

$$G_t(r, \sigma) = \mathcal{N} \begin{cases} \exp(-A^2 r^2), & \text{for } r \leq h_{\text{sml}} \\ 0, & \text{otherwise} \end{cases} \quad (2)$$

where

$$\begin{aligned} \sigma^2 &= \frac{h_{\text{sml}}^2}{8\pi^{1/3}}, \\ A^2 &= \frac{4\pi^{1/3}}{h_{\text{sml}}^2}, \\ \mathcal{N} &= \frac{8}{\pi h_{\text{sml}}^3} \left[ \text{erf}(t) - \frac{2t \exp(-t^2)}{\sqrt{\pi}} \right]^{-1}, \\ t &= 2\pi^{1/6}, \end{aligned} \quad (3)$$

and  $r = h_{\text{sml}}$  is the radius at which the Gaussian kernel is truncated. In smoothed particle hydrodynamics (SPH) simulations,  $h_{\text{sml}}$  is taken to be the gas particle's smoothing length, calculated using a fixed number of nearest-neighbours. In AREPO, gas is discretized in the form of Voronoi cells rather than SPH particles; we therefore define an ‘effective’ smoothing length,  $h_{\text{sml},i}$ , for each gas cell,  $i$ , as

$$h_{\text{sml},i} = f \left( \frac{3m_i}{4\pi\rho_i} \right)^{1/3}, \quad (4)$$

where  $m_i$  and  $\rho_i$ , respectively, are the mass and mass density of the gas cell, and  $f = 4$  is some normalization factor. Our results are insensitive to the precise choice of  $f$ .

By dividing each line of sight into  $N$  bins, we can compute the number density,  $n_{\text{H}}(j)$ , H I-weighted temperature,  $T(j)$ , and H I-weighted peculiar velocity field,  $v(j)$ , at each bin  $j$  (in velocity space) using only the subset of gas cells that intersect each ray. Following exactly the methodology laid out in Theuns et al. (1998), we can then calculate the optical depth,  $\tau(k)$ , for the  $k$ th velocity bin along the line of sight as

$$\begin{aligned} \tau(k) &= \sum_j \sigma_{\alpha} \frac{c}{V_{\text{H}}(j)} n_{\text{H}}(j) \Delta \times \frac{1}{\sqrt{\pi}} \exp \left( - \left[ \frac{v(k) - v(j)}{V_{\text{H}}(j)} \right]^2 \right), \\ V_{\text{H}}^2(j) &= 2k_{\text{B}} T(j)/m_{\text{H}}, \end{aligned} \quad (5)$$

where  $c$  is the speed of light,  $\Delta$  is the width of each bin in units of physical distance,  $x$ , along the line of sight,  $k_{\text{B}}$  is the Boltzmann constant, and  $\sigma_{\alpha} = 4.45 \times 10^{-18} \text{ cm}^2$  is the cross-section of the hydrogen Lyman- $\alpha$  transition. The corresponding transmitted flux is then given by  $F = e^{-\tau}$ , where  $\tau$  is the integrated optical depth along this line of sight.

Due to the considerable uncertainty about the level of photoionization, we follow the standard procedure of rescaling our simulated spectra to the observed optical depth at the corresponding redshifts. At low redshift,  $z \sim 2\text{--}3$ , the rescaling factor is small; at high redshift,  $z \sim 4\text{--}6$ , however, the rescaling becomes increasingly important as fluctuations in the assumed UV background start to become an issue. In particular, at each simulation output, we rescale the optical depths of simulated spectra such that the *mean* transmitted flux matches the *observed* mean flux at that redshift. For the observed mean fluxes, we use the values reported by Walther

<sup>3</sup>We have checked explicitly that our results are converged for this choice for the number of sightlines (see Fig. A2).

et al. (2018) for  $z < 4$  and by Viel et al. (2013) for  $z \geq 4$ . The factors by which the CDM and sDAO spectra are rescaled are not too dissimilar at  $z > 3$ , and are almost identical at lower redshifts (see Fig. 6).

This rescaling procedure is widespread in the simulation community and its validity is worth reflecting on for a moment. As we have mentioned previously, the motivation for rescaling the optical depth is the uncertainty of the photoionization rate. In practice, one assumes that the H I abundance is directly proportional to the photoionization rate and hence, the optical depth can be rescaled by the same factor. The assumption implicitly neglects the following effects, which we consider in turn.

(i) Deviations from equilibrium: These only play an important role during reionization and determine how strongly the gas is being heated. At the redshift of the observations of the Lyman- $\alpha$  forest, the ionization degree should be back in equilibrium. The only remaining effect is the slightly enhanced temperature.

(ii) Collisional ionization: This is a negligible effect at IGM temperatures.

(iii) A constant recombination rate: Since the H I fraction is of order  $\sim 10^{-4}$ , the H II fraction and hence the recombination rate practically do not change for small variations of the H I abundance.

(iv) Spatial fluctuations of the photoionization rate: These disappear quickly after the end of reionization. For very high gas densities, for example in damped Lyman- $\alpha$  systems (DLAs), one would have to take into account self-shielding of gas.

In summary, the rescaling procedure is valid for the optical depths and temperatures of the IGM (see e.g. the discussions in Rauch et al. 1997; Weinberg et al. 1997; Theuns et al. 1998; Bolton et al. 2005). At  $z > 5.5$ , the assumption of a homogeneous photoionization rate fails severely and it is then necessary to perform radiative transfer calculations. The validity of rescaling the mean flux at these high redshifts then becomes questionable. In what follows, we limit our analysis to  $z \leq 5.4$ .

## 4 RESULTS

### 4.1 The clustering of matter

As a precursor to the main analysis in this paper, we show in Fig. 2 the projected gas density map from our simulation volumes at  $z = 5.4$ . The largest panel shows a  $(20 \times 20 \times 4) h^{-1} \text{ cMpc}$  projection from the CDM simulation; the smaller panels zoom into a  $(4 \times 4 \times 2) h^{-1} \text{ cMpc}$  region centred on the most massive halo at this time as it appears in the CDM (upper right) and sDAO (lower right) simulations. While general large-scale filaments and knots look identical in the two density maps, there is noticeable absence of small-scale structure in the sDAO image, in which the gas density distribution is smoother than in CDM. This situation is identical to what is observed in standard WDM simulations, in which the matter distribution is smoothed through free streaming induced by the cut-off in the linear power spectrum, although the mechanism in operation here is collisional Silk damping, rather than free streaming. The smoothed gas distribution in WDM models is manifested as a cut-off in the Lyman- $\alpha$  flux spectrum at small scales; our aim in the subsequent sections is to investigate if the *resurgence* in power at small scales – predicted by models with strong DAOs, but not by thermal relic WDM – can be probed by the Lyman- $\alpha$  forest. Before examining the Lyman- $\alpha$  forest, it is instructive to first look at the DM distribution predicted by these models. Fig. 3 shows ratios (sDAO to CDM) of the non-linear DM power spectrum at  $z = 20, 14, 10, 8$ , and 6 (coloured lines), measured directly from

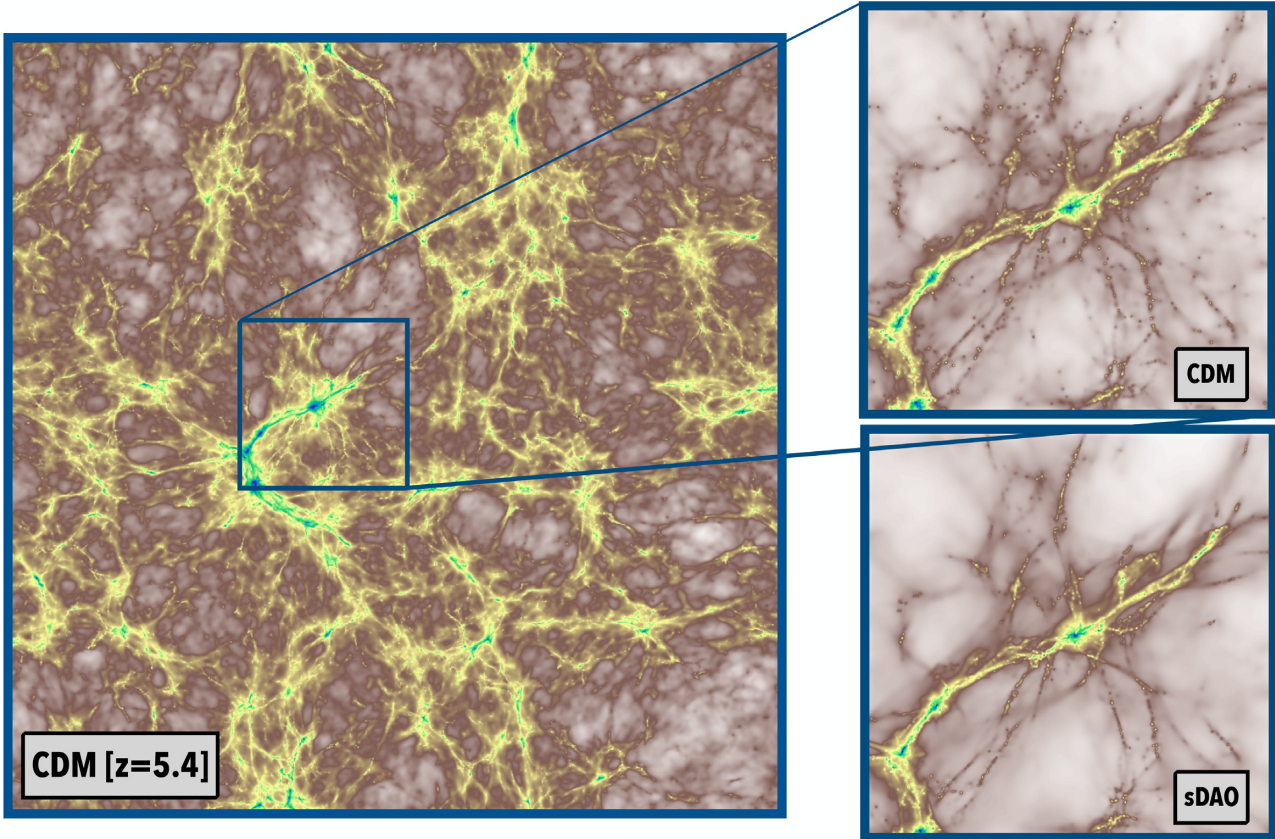


**Figure 2.** Images of the gas density at  $z = 5.4$  obtained from our hydrodynamical simulations. On the left, we project the simulation box along the  $z$ -axis in a projection of comoving dimensions  $(20 \times 20 \times 4) h^{-1} \text{cMpc}$ . The smaller panels zoom into a region centred on the most massive halo at this redshift in a window of size  $(4 \times 4 \times 2) h^{-1} \text{cMpc}$  in CDM (upper right) and the equivalent region in sDAO (lower right). While differences are hard to discern on these scales, the small-scale cut-off in the sDAO model results in a smoother matter distribution than the CDM volume at the same epoch. These images were processed using the publicly available PY-SPHVIEWER package (Benítez-Llambay 2015).

the DM particles in each simulation at the corresponding redshifts. For comparison, we also show, in black, the ratio of the *linear* power spectra in these models, which were used to generate the initial conditions at  $z = 127$ . The ETHOS-4 model, comparable to a 3.3 keV thermal relic, is represented by the dotted lines.

From Fig. 3, one clearly notices that the characteristic DAO peaks are very prominent at early times. At  $z = 20$  and  $z = 14$ , the first DAO peak is still noticeable in the DM distribution (at  $\log [k/h \text{ cMpc}^{-1}] \approx 1.6$ ), but only marginally so by  $z = 10$ . As gravitational collapse continues at  $z < 10$ , increasing the overall power on all scales, the DAO peak is gradually washed away as a result of mode coupling in the (weakly) non-linear regime of structure formation. By  $z = 6$ , any signature of DAOs has completely disappeared – qualitatively, the ratio of the non-linear power spectra looks more similar to an ordinary thermal relic WDM particle. This is consistent with the findings of Buckley et al. (2014) and Vogelsberger et al. (2016), who also noted the absence of acoustic peaks in the DM distribution at relatively high redshifts ( $z \sim 6-8$ ). This is particularly true for the ETHOS-4 model, where the DAOs are nearly absent as early as  $z = 20$  (given the finite resolution of our numerical set-up).

#### 4.2 The Lyman- $\alpha$ forest at a glance

In the top row of Fig. 4 we present the transmitted flux fraction,  $F$ , measured along random lines of sight at  $z = 5$  (left) and  $z =$

4.2 (right) for the CDM and sDAO models. The spectra have been created following the procedure outlined in Section 3.2, after rescaling the mean transmission in each simulation box to the observed transmitted flux. In each case, the lines of sight have been chosen so as to probe the same spatial region in the two simulation volumes. The lower sub-panels show the difference in the transmitted flux,  $\Delta F = F_{\text{CDM}} - F_{\text{sDAO}}$ . This figure highlights the fact that the same line of sight probes different intervening structures in the IGM of the two simulations. In particular, it is clear that, just as in WDM, absorption lines are in general deeper for a random line of sight in the CDM simulation than for the sDAO model, signifying the presence of a more clumpy IGM. This difference is a direct consequence of the cut-off in the initial power spectrum.

The sDAO and CDM models have been rescaled by different amounts when matching the simulated spectra to the observed mean transmitted flux. To disentangle the implications of rescaling from the different line shapes due to the modified cosmology at a given UV background, the middle row of Fig. 4 shows the *unscaled* line-of-sight spectra at  $z = 5$  and  $z = 4.2$ . Clearly, there are residual differences between the two models even in the unscaled case. Quantitatively, these effects are seen more clearly in the bottom row of Fig. 4, which shows the probability distribution function (PDF) of the unscaled transmitted flux for the two models at these redshifts. Considering just CDM to begin with, it is noticeable that as time proceeds, there is a cut-off in the flux PDF at higher values of  $F$ , which comes about due to a combination of two effects:

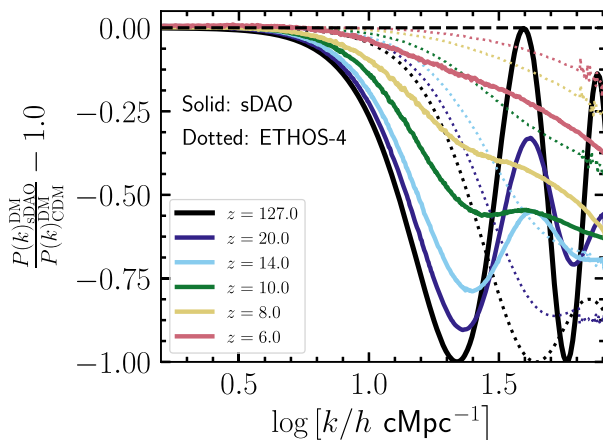


**Figure 3.** Redshift evolution of the ratio of the non-linear matter power spectrum at  $z = 20, 14, 10, 8$ , and  $6$  for the simulations presented in this paper. The power spectra are measured using only the distribution of DM particles in the simulation snapshots. For comparison, we also show the ratio of the *linear* power spectra used as the input to making initial conditions at  $z = 127$ ; we also show results for the ETHOS-4 model with dotted lines. While the matter distribution shows significant differences between the sDAO and CDM models at high redshift (including the signature of DAOs), these differences are suppressed at lower redshifts. In particular, the DAOs are no longer visible in the DM distribution at  $z = 6$ . On the other hand, DAOs are nearly smoothed as early as  $z = 20$  in the ETHOS-4 model due to our finite numerical resolution.

(i) As the universe expands, the background density drops and a given overdensity needs to be larger (in linear dimensions) in order to produce the same signal strength in the Lyman- $\alpha$  forest and (ii) as structure formation proceeds, the non-linear length-scale moves to larger scales, implying that perturbations with larger wavelengths start to collapse, yielding a more structured (clustered) universe. As a result, the extended tail to large  $F$  builds as gravitational collapse proceeds through cosmic time. There is a clear extended tail of high flux in CDM that is less prominent in sDAO. This can be ascribed to the delayed collapse of the first haloes as a result of the suppressed small-scale density fluctuations induced by the DM-radiation coupling in the sDAO model.

A more realistic comparison of the two models is shown in Fig. 5, which displays the *scaled* flux PDFs as a function of redshift. The panels, from top to bottom, show the flux PDFs at  $z = 5, 4.2$ , and  $2$ . This figure highlights a qualitative difference in the manner in which structure formation proceeds in the sDAO model compared to CDM. At  $z = 5$ , for example, the flux PDF is truncated at somewhat lower values of  $F$  than it is in the CDM simulation. This can be ascribed to the delayed collapse of the first haloes as a result of the suppressed small-scale density fluctuations induced by the DM-radiation coupling in the sDAO model. The same difference, though smaller, is also manifested in the flux PDF at  $z = 4.2$ . By  $z = 2$ , however, the flux PDFs are almost indistinguishable between the two models. This is one of the generic features of models that exhibit a primordial cut-off in the linear power spectrum: While the formation of the first galaxies is delayed, structure formation proceeds more rapidly than in CDM afterwards. For the case of WDM, this has been demonstrated in detail in Bose et al. (2016b, 2017). As we show in the following subsection, the same qualitative behaviour is manifested in the 1D flux power spectrum as well.

Fig. 6 displays another way of visualizing the different redshift evolution in the CDM and sDAO models. Here we show the *unscaled* mean transmitted flux as a function of redshift, compared to the observed values that we rescale to. Mean fluxes in the sDAO model are systematically lower at  $z \geq 4$  but nearly identical at later times. Figs 5 and 6 therefore show explicitly the effects of delayed structure formation in the sDAO model, a direct consequence of the intrinsic cut-off in the linear power spectrum.

### 4.3 The 1D flux spectrum

Next, we investigate if the distinctive feature of the sDAO model, the small-scale acoustic oscillation, is detectable in the Lyman- $\alpha$  forest. To probe this feature, we compute the 1D Lyman- $\alpha$  flux power spectrum. Following Viel et al. (2013), at redshift  $z$ , we compute the power spectrum,  $P_{1D}(k)$ , of the *fractional transmission*,  $\delta_F(z)$ , which is defined as

$$\delta_F(z) = \frac{F(z) - \langle F(z) \rangle}{\langle F(z) \rangle} \quad (6)$$

where  $\langle F(z) \rangle$  is the mean transmitted flux at redshift  $z$ . As described in Section 3.2, the mean flux at every snapshot is rescaled to match the observed mean flux at that redshift. The power spectrum is calculated in this way for each of the 1024 lines of sight at a given redshift; the resulting value of  $P_{1D}(k)$  at that redshift is then obtained by taking the mean value of the individual power spectra at each  $k$  mode.

Fig. 7 shows the results of this procedure for the CDM and sDAO simulations over a range of redshifts. Each of the models is represented by a shaded region that denotes the uncertainty in observed mean transmission at that redshift reported by Viel et al. (2013;  $z \geq 4$ ) and Walther et al. (2018;  $z < 4$ ), which we have propagated through to the normalization of the simulated power spectra. In each panel we also display the observed flux spectra at each redshift, with data compiled by Kim et al. (2004), Viel et al. (2013), Iršič et al. (2017b), and Walther et al. (2018) from the MIKE/HIRES and XQ-100 quasar spectra samples. We do not include large-scale flux power spectrum measurements from BOSS (Palanque-Delabrouille et al. 2013) as the CDM and sDAO models are identical on these scales ( $k \lesssim 0.02 \text{ s km}^{-1}$ ).

The redshift evolution of the flux power spectra is reminiscent of the behaviour seen in Figs 3 and 5, in which the stark differences between the CDM and sDAO models diminish with redshift. For example, at  $z = 5.4$  the power spectra for the two models match only on the very largest scales ( $k \leq 0.2 \text{ s km}^{-1}$ ); in contrast, their power spectra are identical across all scales by  $z = 2$ .

While the flux power spectra measurements at  $z \leq 4.6$  obtained from the CDM simulation are in good agreement with the data even at the smallest scales (at least within the errors afforded by the uncertainty in the mean transmitted flux), this is not so for the two highest redshift bins ( $z = 5, 5.4$ ). In particular, the simulated flux power spectra show a sharper decrement of power than is observed at scales smaller than  $k \sim 0.07 \text{ s km}^{-1}$ . Part of this discrepancy may be due to incomplete masking of metal lines, which could add artificial power at small scales. This effect would be more pronounced at a higher redshift where masking all metal contributions is more challenging (e.g. Walther et al. 2018). The bulk of the discrepancy, however, can be pinpointed to numerical resolution, as shown explicitly in the convergence tests performed by Bolton et al. (2017; see their fig. A4). These authors show that at  $z \sim 5$ , a simulation where each gas element is  $\sim 10^6 M_\odot$  (similar to ours) can show a deficit of small-scale power of around 30 per cent at  $k \sim 0.1 \text{ s km}^{-1}$ .

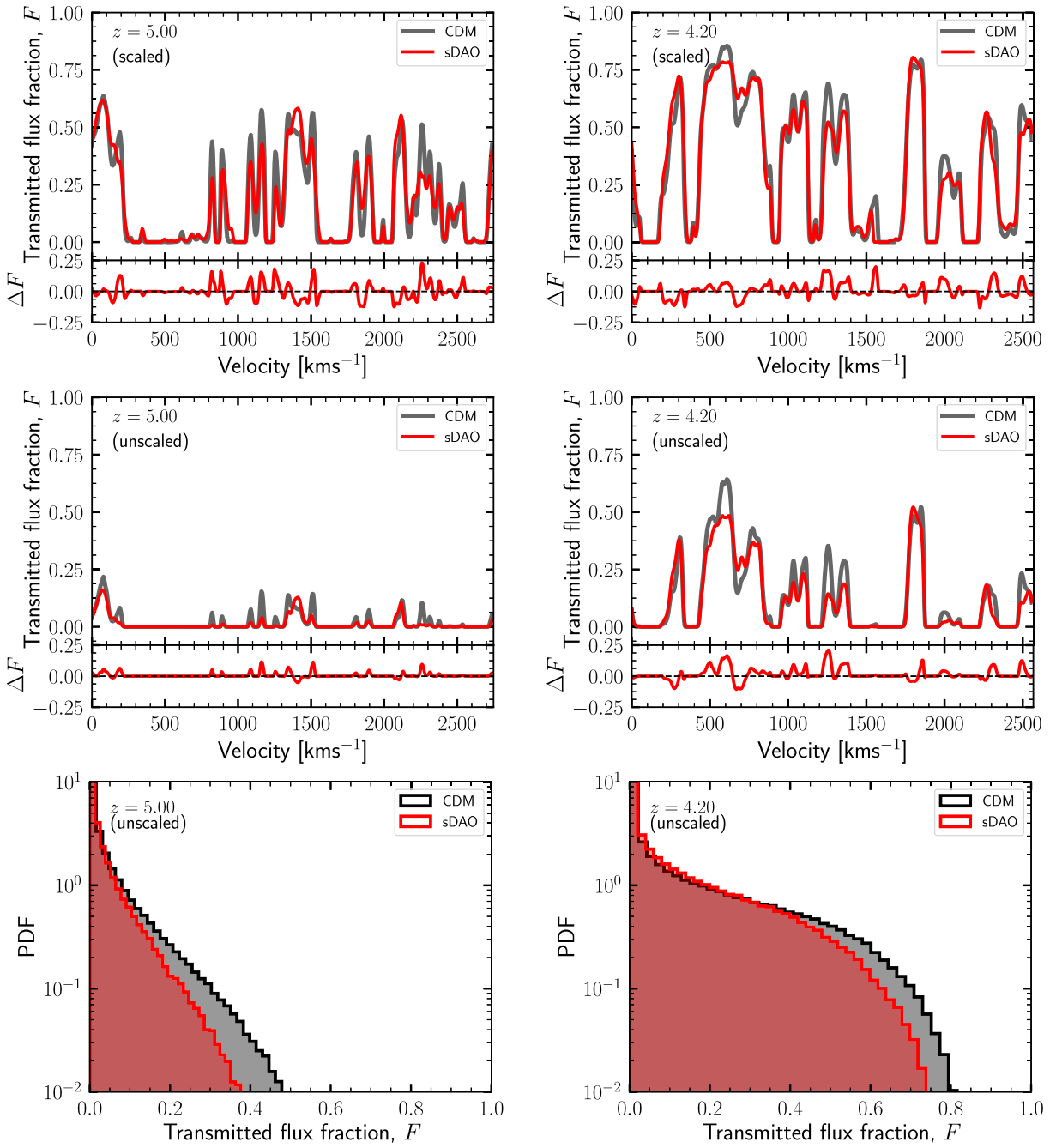


**Figure 4.** Top row: synthetic mock spectra extracted from our simulations at  $z = 5$  (left) and  $z = 4.2$  (right). Each panel shows the transmitted flux fraction,  $F$ , in velocity space for a specific randomly selected line of sight through the simulation volume at the corresponding redshift. The lines of sight are chosen such that the same spatial region is probed in the CDM (black) and sDAO (red) simulation volumes. Clearly, more intervening structure can be inferred from the CDM spectra as evidenced by the deeper transmission lines than in sDAO. The lower panels show the relative difference in transmitted flux, i.e.  $\Delta F = F_{\text{CDM}} - F_{\text{sDAO}}$ . Middle row: The same lines of sight shown in the top row but before we rescale the mean flux to the observed values. Bottom row: The unscaled flux PDF at these redshifts. These panels show the ‘true’ difference in the transmitted flux between the CDM and sDAO models, i.e. by removing any artefacts that may be brought in by the different amount of rescaling required for the two DM models.

compared to a higher resolution simulation with 8 times better mass resolution. This difference diminishes with redshift. Given that we are mostly interested in the *relative* difference between the CDM and sDAO models, however, this difference is not critical; the comparison with observations serves mainly as a consistency check of our procedure for generating mock spectra from our simulations.

Bearing in mind that higher resolution only increases the small-scale power by 10–30 per cent, Fig. 7 shows that the sDAO model is in clear tension with the data on scales smaller than  $k \sim 0.04 \text{ s km}^{-1}$  at  $z \lesssim 4.6$ . This is expected, considering that the linear theory cut-off in the sDAO model is similar to that of a 1.6 keV thermal relic, which may already be ruled out by existing Lyman- $\alpha$  constraints (e.g. Viel et al. 2013; Baur et al. 2016). However, as we

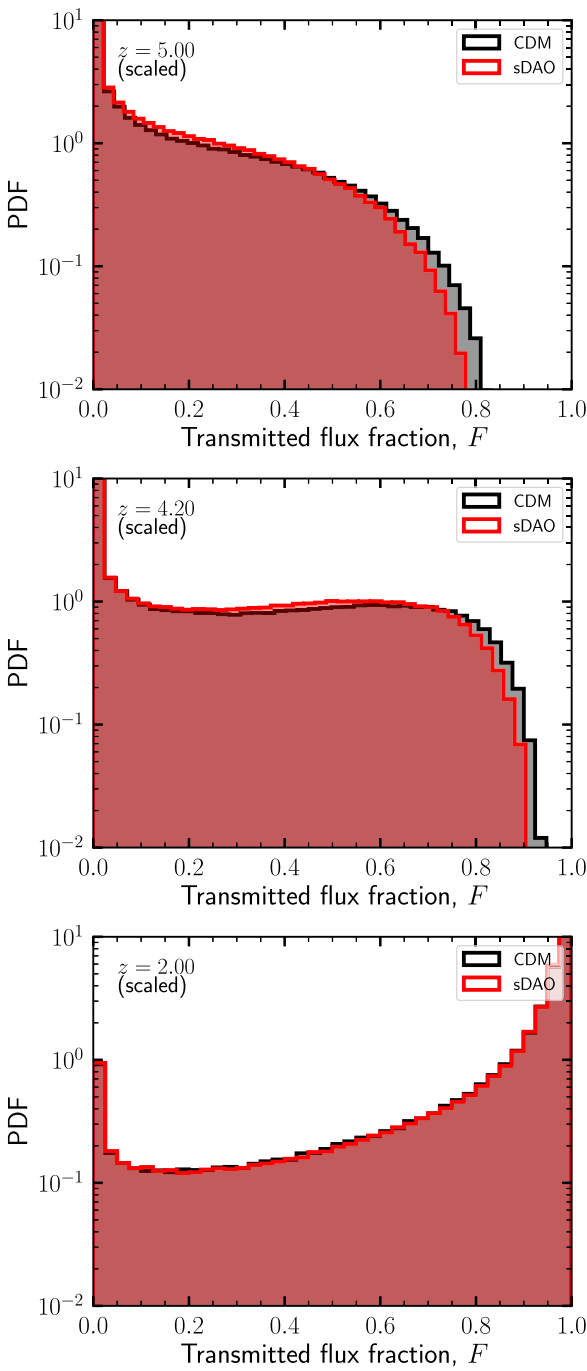


**Figure 5.** Comparison of the PDF of the transmitted flux,  $F$ , at  $z = 5, 4.2$ , and  $2$  (top to bottom) after rescaling the mean transmitted flux. While both CDM and sDAO show identical PDFs at low redshift, the CDM simulations display an extended tail of high flux at higher redshift.

have remarked in Section 1, constraining models against observed data by means of their relative normalization is fraught with uncertainties due to the assumed thermal history of the IGM. We are therefore cautious of our interpretation of Fig. 7 with this caveat in mind.

In Fig. 8 we show the redshift evolution of the ratio of the (mean) flux spectra. This figure reveals the defining characteristics of the sDAO model. At  $z \lesssim 4.2$ , the behaviour relative to CDM is similar to what is observed in the case of WDM-like models: agreement

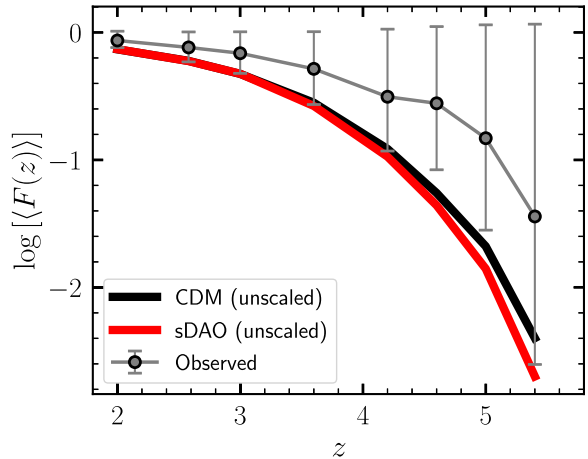
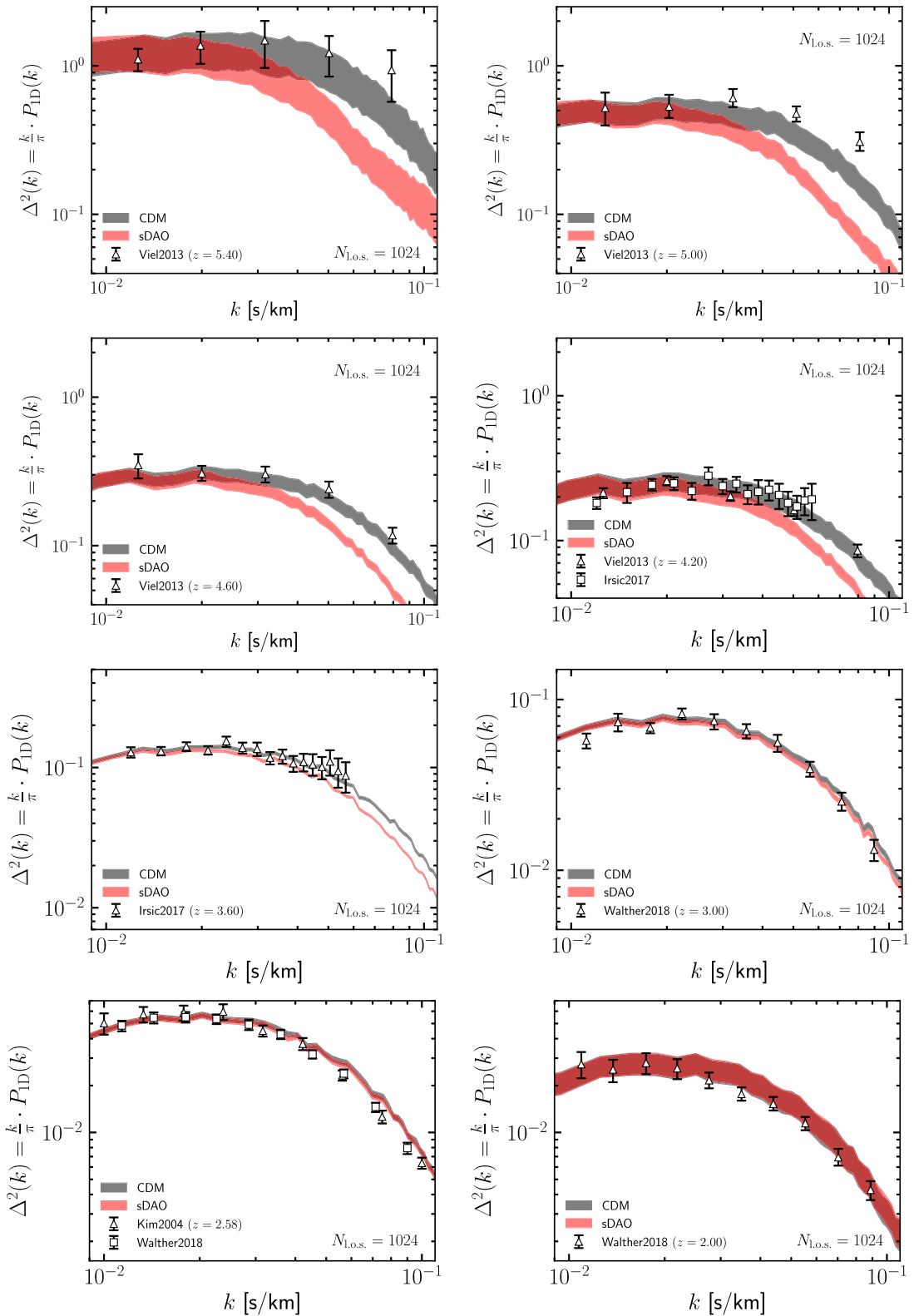


**Figure 6.** Redshift evolution of the (unscaled) mean transmitted flux in the two DM models compared to the observed value of the mean transmission at each redshift. While sDAO spectra are rescaled by a larger factor than CDM spectra at  $z \gtrsim 4$ , the rescaling is almost identical towards lower redshifts. Data were obtained from Viel et al. (2013) and Walther et al. (2018).

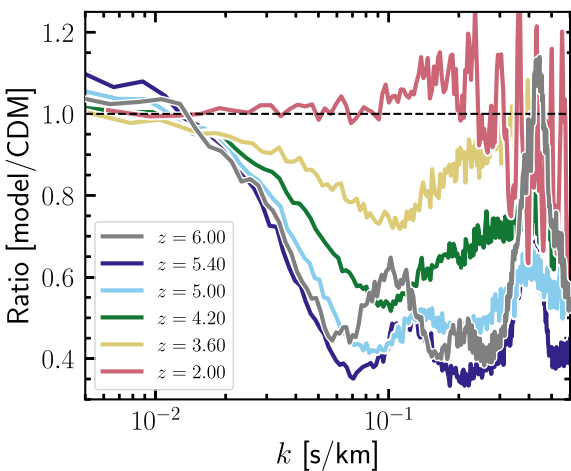
with CDM on large scales,<sup>4</sup> followed by largely suppressed power below some characteristic scale. At  $z \gtrsim 5$ , however, a ‘bump’ develops at  $k \sim 0.13 \text{ s km}^{-1}$ , which becomes increasingly prominent at higher redshifts. This is, indeed, the imprint of the DAO in the gas distribution at these early times. This feature is even more prominent at  $z = 6$ , where even the *second* DAO is visible at  $k \sim 0.2 \text{ s km}^{-1}$ . In contrast, the ‘bump’ at  $k \sim 0.4 \text{ s km}^{-1}$  that becomes increasingly prominent towards high redshifts is most likely a numerical effect associated with the finite resolution in our simulations, which affects different cosmologies differently. As the overall power increases across all scales between  $z = 6$  to  $z = 5.4$ , mode coupling due to the (mildly) non-linear evolution erases the second DAO bump and transfers its power to smaller and larger scales. As a result, the first DAO peak moves towards smaller scales. Note that the flux spectrum at  $z = 6$  is shown simply for comparison, and does not necessarily represent the true ratio at this redshift, where the rescaling procedure may no longer be valid due to incomplete reionization (see the discussion in Section 3.2).

Fig. 8 reveals the value of the Lyman- $\alpha$  flux spectrum as a probe of small-scale clustering: While the 3D DM distribution showed no evidence of DAOs at  $z \lesssim 10$  (Fig. 3), the linear scales probed by the flux power spectrum bears memory of the acoustic oscillations in the linear power spectrum of the sDAO model. This may be because the 1D flux spectrum, which can be qualitatively understood as an integrated version of the 3D power spectrum along the line of sight, weighted by velocity moments, is more sensitive to small-scale features in the linear power spectrum than the 3D clustering. This is somewhat reminiscent of modified theories of gravity [e.g. the  $f(R)$  gravity model], in which the velocity divergence power spectrum (an integral of motion) has been shown to be a much more sensitive probe of deviations from standard gravity than simply the matter density field (e.g. Jennings et al. 2012; Bose, Hellwing & Li 2015). We leave a full understanding of the comparison between 1D and 3D power spectra for future work.

<sup>4</sup>The increased power on large scales in sDAO compared to CDM is simply an artefact of rescaling the mean flux. As the small-scale power is suppressed heavily in the sDAO simulation, the large-scale power is boosted somewhat in order to achieve the same mean flux in the two models.



**Figure 7.** The 1D Lyman- $\alpha$  flux spectra for CDM and sDAO, compared to data obtained from MIKE/HIRES and XQ-100 quasar spectra at  $z = 5.4, 5, 4.6, 4.2, 3.6, 3, 2.58$ , and  $2$ . To construct the simulated power spectra, we have, where possible, attempted to match the path length of the observed spectra. Each simulated spectrum makes use of 1024 lines of sight. The observational measurements are obtained from data compiled by Kim et al. (2004), Viel et al. (2013), Iršič et al. (2017b), Walther et al. (2018). The shaded regions encompass the reported uncertainty in observed mean transmission at that redshift, which translates to an uncertainty in the normalization of the power spectra after rescaling.



**Figure 8.** Ratio of the mean flux power spectra [ $\Delta_{\text{sDAO}}^2(k)/\Delta_{\text{CDM}}^2(k)$ ]. For clarity, we do not show the observational data in this figure. The signature of DAOs (at  $k = 0.4 \text{ s km}^{-1}$ ) can be noticed in the high-redshift spectra, particularly at  $z = 6$  and  $z = 5.4$ . Any evidence of DAOs is completely washed out by  $z = 2$ . Note that the ‘bump’ at  $k \sim 0.4 \text{ s km}^{-1}$  is numerical, and is set by the finite resolution of our simulation set-up. This secondary feature is not sourced by DAOs.

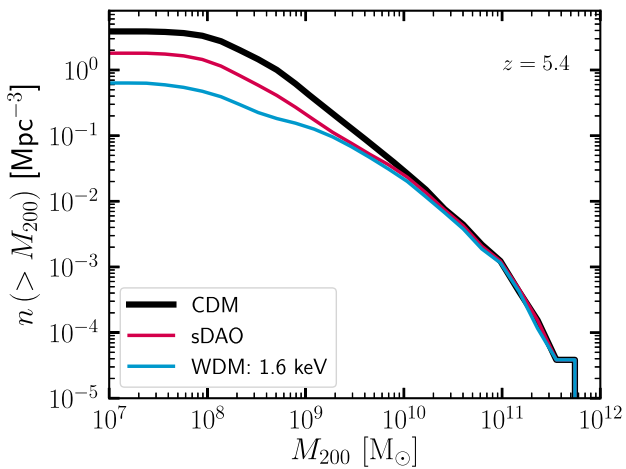


**Figure 9.** Comparison of the cumulative halo mass functions at  $z = 5.4$  for the CDM, sDAO, and 1.6 keV thermal relic models. While both the sDAO and WDM models begin to deviate from CDM at a similar mass scale, there is more small-scale power in sDAO. The noticeable upturn at  $M_{200} \sim 3 \times 10^8 \text{ M}_\odot$  in the WDM mass function is the tell-tale signature of artificial fragmentation (Wang & White 2007); this is largely absent in the sDAO model.

It is illuminating to consider the difference in structure in the sDAO and WDM models at these early times in greater detail. Fig. 9 compares the (cumulative) halo mass function in CDM, sDAO, and 1.6 keV cosmologies at  $z = 5.4$ . In this calculation, halo mass is defined by  $M_{200}$ , which is the mass contained within  $r_{200}$ , the radius interior to which the mean density is equal to 200 times the critical density of the universe at that redshift. As expected, all three models agree on the abundance of the most massive haloes in the volume at these times ( $M_{200} > 10^{10} \text{ M}_\odot$ ). Both the sDAO and WDM models then peel away from the CDM curve at an identical mass scale; this is a direct consequence of the fact that the linear power spectra of these two models also deviate from CDM at identical scales. There is, however, a clear excess (of around a factor of 3) of

haloes with  $M_{200} < 3 \times 10^9 \text{ M}_\odot$  in sDAO compared to the 1.6 keV simulation. This excess of power is sourced by the DAO, whereas the initial density fluctuations are suppressed indefinitely in the case of WDM. It is also interesting to note that while the effects of artificial halo formation are clear in the WDM case (as evidenced by the unnatural ‘upturn’ in the mass function at  $M_{200} \sim 3 \times 10^8 \text{ M}_\odot$ ; Wang & White 2007), the manifestation of these spurious haloes seems largely reduced in the sDAO model, in which any spurious halo formation is outnumbered by haloes that have collapsed out of true gravitational instability.

The left-hand panel of Fig. 10 compares the relative difference of the flux spectra to CDM in the two models at  $z = 5.4$ . Power on scales larger than  $k \sim 0.05 \text{ s km}^{-1}$  is suppressed by an almost identical amount, but the behaviour of the two models is different on smaller scales. In particular, while power continues to be suppressed in the case of the 1.6 keV thermal relic, the cut-off in the power is halted by the development of the DAO bump around  $k \sim 0.13 \text{ s km}^{-1}$ , which is only present in the sDAO model and not in the WDM model. In practice, this may prove to be difficult to observe since the largest signal is expected to be present at the highest redshift, where the UV background starts to be inhomogeneous due to incomplete reionization.

We also show predictions for the ETHOS-4 model in which the cut-off is on a smaller scale than in the sDAO case, and where the first DAO peak is of lower amplitude than in sDAO and is pushed to smaller scales (see Fig. 1). The DAO feature in ETHOS-4 is thus unresolved by our simulation (the numerical set-up was selected to just resolve the first sDAO peak). Regardless, this comparison highlights the potential of 1D flux spectrum measurements to distinguish not only non-CDM models from CDM, but also different non-CDM models from each other. The major constraining power comes from scales smaller than  $k \sim 0.08 \text{ s km}^{-1}$ , where there is only limited data available at the moment (but see Boera et al. 2019 for newer data reaching to somewhat smaller scales).

One may be concerned that the DAO features we have identified in the  $z = 5.4$  flux power spectrum may be affected by the small-scale noise manifest as the artificial peak at  $k \sim 0.4 \text{ s km}^{-1}$ . To diagnose this, in the right-hand panel of Fig. 10 we show the evolution of the flux power-spectrum ratio from  $z = 5.4$  to  $z = 4.2$  for the sDAO and 1.6 keV WDM models. At  $z = 5.4$ , the DAO is very prominently present in the sDAO case while it is of course absent for the 1.6 keV model; on the other hand, the behaviour of the two models is almost identical by  $z = 4.2$ . This is consistent with the picture in Fig. 8: The second DAO, which was visible at  $z = 6$ , is smoothed away by  $z = 5.4$  due to non-linear mode coupling; similarly, the first DAO bump, which is visible at  $z = 5.4$ , is smeared away by  $z = 4.2$ . This is because the overall power across all scales increases towards lower redshifts, giving the illusion of the DAO peaks being smeared with the numerical ‘noise peak’ as time progresses. The effects of noise in the flux power spectrum are manifested more strongly in the 1.6 keV WDM case as there is a lack of ‘real’ power on small scales, in contrast to the sDAO model where the acoustic oscillation adds physical power on a level larger than the noise at  $k > 0.1 \text{ s km}^{-1}$ .

How the noise level shifts as a function of resolution (see also Viel et al. 2013) may be evaluated by comparing the  $z = 5.4$  flux spectra for the sDAO model at low and high resolution (grey and red curves, respectively). At the lower resolution, the numerical bump is shifted to larger scales by a factor of 2 (as expected, since the low-resolution simulation retains the same number of particles in a box that is twice as big as the high-resolution simulation). Moreover, the DAO bump, which just starts to develop, blends with the numerical bump and is therefore unresolved in the low-resolution simulation.

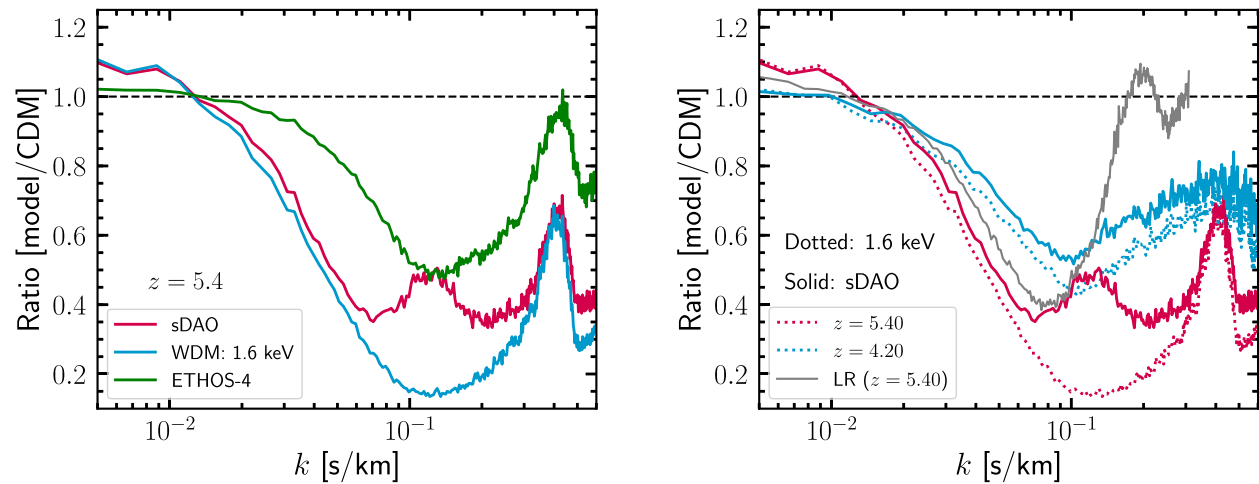


**Figure 10.** *Left-hand panel:* as Fig. 8, but now comparing the sDAO model with the 1.6 keV WDM and ETHOS-4 models at  $z = 5.4$ . The qualitative behaviour of each model is similar on scales larger than  $k = 0.1 \text{ s km}^{-1}$ , in that power is suppressed relative to CDM. On smaller scales, the sDAO model exhibits a prominent bump induced by the first DAO peak. This feature is not observed in ETHOS-4, which also exhibits DAOs in the linear power spectrum, but of smaller amplitude than in the sDAO case. Each model has been run at the same resolution and each curve therefore exhibits the same numerical ‘bump’ at  $k = 0.4 \text{ s km}^{-1}$ . *Right-hand panel:* the evolution of the flux spectrum ratio from  $z = 5.4$  to  $z = 4.2$  for the sDAO (solid lines) and 1.6 keV WDM models (dotted lines). The  $z = 5.4$  flux spectrum ratio in the low-resolution (LR) sDAO simulation is shown in grey. As time progresses, the overall increase of power causes adjacent modes to couple non-linearly, thus erasing any sharp (DAO) features in the power spectrum, until  $z = 4.2$  where the behaviour of the sDAO and 1.6 keV WDM models is very similar.

With increased resolution (i.e. in our default simulations), the DAO is resolved before the noise becomes dominant. Thus, this figure reassures us that our physical interpretation of the first peak in the  $z = 5.4$  flux spectrum for the sDAO model is not affected strongly by numerical systematics. As in the case of the cut-off in the small-scale flux spectrum, it may be that quantitative details in Fig. 10 are affected by assumptions made for the thermal history of the IGM. While varying these assumptions may certainly smear the prominence of the DAO feature, it is not clear that such bumps could be replicated by baryonic mechanisms. In particular, the scale at which these features are manifested, if induced by the nature of the DM, will be set by processes intrinsic to the DM model. We leave a detailed investigation of degeneracies between DAOs and thermal histories to future work.

## 5 CONCLUSIONS

We have performed detailed hydrodynamical simulations of non-standard dark matter species in which the DM is coupled to a relativistic component in the early universe. These interactions alter the primordial linear power spectrum predicted by the concordance cosmological model in a distinctive way: by generating a cut-off at the scale of dwarf galaxies through collisional damping, followed subsequently by a series of ‘dark acoustic oscillations’ (DAOs) towards smaller scales (see Fig. 1). Early structure formation in these models is therefore modified considerably from standard cold dark matter, principally in the form of a delay in the formation of the first stars, and a suppression in the abundance of low-mass galaxies (e.g. Lovell et al. 2018). The structure of DM haloes may be modified as well through strong DM self-interactions at late times that reshape the phase-space density profiles of galactic haloes (e.g. Vogelsberger et al. 2016). The extents to which these processes impact galaxy formation are, of course, sensitive to parameters specific to the DM theory, such as the duration of DM–radiation coupling, or the self-interaction cross-section.

While it is impossible to explore this parameter space fully, various permutations of these model parameters will predict largely similar galactic populations. The ETHOS framework (Cyr-Racine et al. 2016) provides a formalism for mapping these DM properties to ‘effective’ parameters that shape structure formation, thereby providing a flexible way to explore the implications of a vast range of theories on galaxy formation. In this paper, we focus our attention on an atomic DM model (which we refer to as sDAO) in which DM is composed of two massive fermions that are oppositely charged under a new unbroken  $U(1)$  dark gauge force (see Section 2). The linear matter power spectrum of this model has a cut-off relative to CDM at  $k \sim 10 \text{ h cMpc}^{-1}$ , identical to a warm dark matter thermal relic with mass 1.6 keV, but differs from WDM on smaller scales where it is composed of a significant number of undamped DAOs. While models as extreme as these may already be strongly constrained, our goal in this paper was to investigate if DAOs may be, in principle, detectable in the Lyman- $\alpha$  forest, rather than to present a model that matches the available data. A priori, it is not obvious that DAOs would persist in the Lyman- $\alpha$  flux spectrum. In particular, we sought to identify observational proxies that are able to distinguish between the different small-scale behaviour of these DAO models from WDM. For this purpose, we have investigated the statistics of the Lyman- $\alpha$  forest extracted from hydrodynamical simulations performed with these models using the AREPO code (Springel 2010) coupled with a sophisticated galaxy formation model used as part of the IllustrisTNG project (Marinacci et al. 2018; Naiman et al. 2018; Nelson et al. 2018; Pillepich et al. 2018b; Springel et al. 2018).

Our main conclusions from the current study are as follows.

- (i) On scales smaller than  $k \sim 4 \text{ h cMpc}^{-1}$ , the 3D distribution of DM is clustered less strongly in the sDAO model than in CDM, although the differences get smaller with time (Fig. 3). In particular, while there is a strong DAO signature imprinted in the matter

distribution at  $z \geq 10$ , further epochs of gravitational collapse wash away this feature entirely by  $z \sim 6$ .

(ii) A random line of sight through the sDAO simulation box reveals far less structure in absorption than the equivalent line of sight in the CDM simulation (Fig. 4). This is a direct consequence of the cut-off in the primordial power spectrum in the sDAO model, delaying the formation of galaxies at these high redshifts ( $z \gtrsim 3$ ).

(iii) Despite the delayed start to the galaxy formation process in the sDAO model, it catches up with CDM by  $z \approx 2$ . This faster growth of structure is a fairly generic phenomenon observed in models with a cut-off in the linear power spectrum (including WDM). In our work, this is manifested in the form of the transmitted flux PDFs (Fig. 5), which are truncated towards high values in the sDAO model at  $z \geq 4$ , but are identical to CDM by  $z = 2$ . The probability that a given line of sight intersects a region with high transmitted flux increases as the universe transitions from neutral to ionized due to the ionizing radiation from high-redshift galaxies.

(iv) While the 1D flux power spectra are identical in CDM and in the sDAO model at  $z \leq 3$ , there are significant differences at higher redshifts. In fact, present data at these redshifts already place the sDAO in significant tension with observations (Fig. 7), although astrophysical systematics may relax the level of discrepancy.

(v) More interestingly, however, we find that the DAO bump characteristic of the sDAO model – which was absent in the 3D matter distribution – is imprinted prominently in the 1D flux power spectrum at  $z \geq 5$  on scales smaller than  $k \sim 0.1 \text{ s km}^{-1}$  (Fig. 8). At  $z \leq 4.2$ , the DAO feature is smoothed out, and the behaviour of the model is then reminiscent of standard WDM.

(vi) The appearance and disappearance of the DAO at different redshifts therefore offers an opportunity to disentangle small-scale features in the flux power spectrum induced by the nature of DM from astrophysical effects (e.g. different reionization histories). In particular, precise measurements of the flux power spectrum on scales smaller than  $k \approx 0.1 \text{ s km}^{-1}$  will be fundamental to distinguishing different DM models from each other (Fig. 10).

While there is a vast parameter space of well-motivated non-standard CDM models, the predictions they make for the formation of structure and the properties of galaxies can be challenging to differentiate. Of fundamental importance is the need to identify sets of statistics that allow the identification of *physical* scales that are characteristic of these theories. DM models in which there is a coupling to a relativistic species in the early Universe are characterized in the linear regime by a cut-off at the scale of dwarf galaxies followed by a series of dark acoustic oscillations towards smaller scales. In this work we have shown that these fundamental scales, while absent in the total matter distribution after the epoch of reionization, are imprinted in the 1D Lyman- $\alpha$  flux power spectrum in a way that may be constrained with future high-precision observations. In the meantime, it is interesting to consider further statistics that could reveal the scale-dependent behaviour of different DM theories; possible examples include the clustering of DLAs and Lyman-limit systems or cross-correlations of Lyman- $\alpha$  with galaxy properties.

## ACKNOWLEDGEMENTS

We thank the anonymous referee for providing suggestions that have improved this manuscript. We are very grateful to Volker Springel for allowing us access to AREPO, which was used to run all the simulations used in this paper. SB is supported by Harvard

University through the ITC Fellowship. MV acknowledges support through an MIT RSC award, a Kavli Research Investment Fund, NASA ATP grant NNX17AG29G, and NSF grants AST-1814053 and AST-1814259. JZ and Sebastian Bohr acknowledge support by a Grant of Excellence from the Icelandic Research Fund (grant number 173929–051). CP acknowledges support by the European Research Council under ERC-CoG grant CRAGSMAN-646955. F-Y C-R acknowledges the support of the National Aeronautical and Space Administration ATP grant NNX16AI12G at Harvard University. This work was made possible in part by usage of computing resources at the University of Southern Denmark through the NeIC Dellingr resource sharing pilot. A fraction of the simulations in this work were carried out on the Garpur supercomputer, a joint project between the University of Iceland and University of Reykjavík with funding from Rannís.

## REFERENCES

Ackerman L., Buckley M. R., Carroll S. M., Kamionkowski M., 2009, *Phys. Rev. D*, 79, 023519  
 Albert A. et al., 2017, *ApJ*, 834, 110  
 Altay G., Theuns T., 2013, *MNRAS*, 434, 748  
 Aprile E. et al., 2018, *Phys. Rev. Lett.*, 121, 111302  
 Bartels R., Krishnamurthy S., Weniger C., 2016, *Phys. Rev. Lett.*, 116, 051102  
 Baur J., Palanque-Delabrouille N., Yèche C., Magneville C., Viel M., 2016, *J. Cosmol. Astropart. Phys.*, 8, 012  
 Benitez-Llambay A., 2015, py-sphviewer: Py-SPHViewer v1.0.0. <http://dx.doi.org/10.5281/zenodo.21703>  
 Bode P., Ostriker J. P., Turok N., 2001, *ApJ*, 556, 93  
 Böhm C., Riazuelo A., Hansen S. H., Schaeffer R., 2002, *Phys. Rev. D*, 66, 083505  
 Böhm C., Schewtschenko J. A., Wilkinson R. J., Baugh C. M., Pascoli S., 2014, *MNRAS*, 445, L31  
 Boera E., Becker G. D., Bolton J. S., Nasir F., 2019, *ApJ*, 872, 101  
 Bolton J. S., Haehnelt M. G., Viel M., Springel V., 2005, *MNRAS*, 357, 1178  
 Bolton J. S., Puchwein E., Sijacki D., Haehnelt M. G., Kim T.-S., Meiksin A., Regan J. A., Viel M., 2017, *MNRAS*, 464, 897  
 Bond J. R., Szalay A. S., 1983, *ApJ*, 274, 443  
 Bose S., Hellwing W. A., Li B., 2015, *J. Cosmol. Astropart. Phys.*, 2, 034  
 Bose S., Hellwing W. A., Frenk C. S., Jenkins A., Lovell M. R., Helly J. C., Li B., 2016a, *MNRAS*, 455, 318  
 Bose S., Frenk C. S., Hou J., Lacey C. G., Lovell M. R., 2016b, *MNRAS*, 463, 3848  
 Bose S. et al., 2017, *MNRAS*, 464, 4520  
 Boylan-Kolchin M., Bullock J. S., Kaplinghat M., 2011, *MNRAS*, 415, L40  
 Bozek B. et al., 2019, *MNRAS*, 483, 4086  
 Brinckmann T., Zavala J., Rapetti D., Hansen S. H., Vogelsberger M., 2018, *MNRAS*, 474, 746  
 Bringmann T., Ihle H. T., Kersten J., Walia P., 2016, *Phys. Rev. D*, 94, 103529  
 Buckley M. R., Zavala J., Cyr-Racine F.-Y., Sigurdson K., Vogelsberger M., 2014, *Phys. Rev. D*, 90, 043524  
 Buen-Abad M. A., Marques-Tavares G., Schmaltz M., 2015, *Phys. Rev. D*, 92, 023531  
 Bullock J. S., Boylan-Kolchin M., 2017, *ARA&A*, 55, 343  
 Carlson E. D., Machacek M. E., Hall L. J., 1992, *ApJ*, 398, 43  
 Chacko Z., Cui Y., Hong S., Okui T., Tsai Y., 2016, *J. High Energy Phys.*, 12, 108  
 Chu X., Dasgupta B., 2014, *Phys. Rev. Lett.*, 113, 161301  
 Cole S. et al., 2005, *MNRAS*, 362, 505  
 Colín P., Avila-Reese V., Valenzuela O., 2000, *ApJ*, 542, 622  
 Colín P., Avila-Reese V., Valenzuela O., Firmani C., 2002, *ApJ*, 581, 777  
 Colless M. et al., 2001, *MNRAS*, 328, 1039

Creasey P., Sameie O., Sales L. V., Yu H.-B., Vogelsberger M., Zavala J., 2017, *MNRAS*, 468, 2283

Croft R. A. C., Weinberg D. H., Katz N., Hernquist L., 1998, *ApJ*, 495, 44

Croft R. A. C., Weinberg D. H., Pettini M., Hernquist L., Katz N., 1999, *ApJ*, 520, 1

Cyr-Racine F.-Y., Sigurdson K., 2013, *Phys. Rev. D*, 87, 103515

Cyr-Racine F.-Y., de Putter R., Raccanelli A., Sigurdson K., 2014, *Phys. Rev. D*, 89, 063517

Cyr-Racine F.-Y., Sigurdson K., Zavala J., Bringmann T., Vogelsberger M., Pfrommer C., 2016, *Phys. Rev. D*, 93, 123527

Das S., Mondal R., Rentala V., Suresh S., 2018, *J. Cosmol. Astropart. Phys.*, 1808, 045

Davé R., Spergel D. N., Steinhardt P. J., Wandelt B. D., 2001, *ApJ*, 547, 574

Daylan T., Finkbeiner D. P., Hooper D., Linden T., Portillo S. K. N., Rodd N. L., Slatyer T. R., 2016, *Phys. Dark Universe*, 12, 1

de Blok W. J. G., McGaugh S. S., Bosma A., Rubin V. C., 2001, *ApJ*, 552, L23

Di Cintio A., Brook C. B., Macciò A. V., Stinson G. S., Knebe A., Dutton A. A., Wadsley J., 2014, *MNRAS*, 437, 415

Díaz Rivero A., Dvorkin C., Cyr-Racine F.-Y., Zavala J., Vogelsberger M., 2018, *Phys. Rev. D*, 98, 103517

Dooley G. A., Peter A. H. G., Vogelsberger M., Zavala J., Frebel A., 2016, *MNRAS*, 461, 710

Dubois Y. et al., 2014, *MNRAS*, 444, 1453

Eisenstein D. J. et al., 2005, *ApJ*, 633, 560

Elbert O. D., Bullock J. S., Garrison-Kimmel S., Rocha M., Oñorbe J., Peter A. H. G., 2015, *MNRAS*, 453, 29

Faucher-Giguère C.-A., Lidz A., Zaldarriaga M., Hernquist L., 2009, *ApJ*, 703, 1416

Feng J. L., Kaplinghat M., Tu H., Yu H.-B., 2009, *J. Cosmol. Astropart. Phys.*, 0907, 004

Fermi-LAT Collaboration, 2017, preprint ([arXiv:1705.00009](https://arxiv.org/abs/1705.00009))

Fitts A. et al., 2017, *MNRAS*, 471, 3547

Flores R. A., Primack J. R., 1994, *ApJ*, 427, L1

Garzilli A., Boyarsky A., Ruchayskiy O., 2017, *Phys. Lett. B*, 773, 258

Garzilli A., Magalich A., Theuns T., Frenk C. S., Weniger C., Ruchayskiy O., Boyarsky A., 2018, preprint ([arXiv:1809.06585](https://arxiv.org/abs/1809.06585))

Gnedin N. Y., Hui L., 1998, *MNRAS*, 296, 44

Hahn O., Abel T., 2011, *MNRAS*, 415, 2101

Hooper D., Goodenough L., 2011, *Phys. Lett. B*, 697, 412

Ibata R. A., Ibata N. G., Famaey B., Lewis G. F., 2014, *Nature*, 511, 563

Iršič V. et al., 2017b, *MNRAS*, 466, 4332

Iršič V., Viel M., Haehnelt M. G., Bolton J. S., Becker G. D., 2017a, *Phys. Rev. Lett.*, 119, 031302

Jennings E., Baugh C. M., Li B., Zhao G.-B., Koyama K., 2012, *MNRAS*, 425, 2128

Jungman G., Kamionkowski M., Griest K., 1996, *Phys. Rep.*, 267, 195

Kaplan D. E., Krnjaic G. Z., Rehmann K. R., Wells C. M., 2010, *J. Cosmol. Astropart. Phys.*, 1005, 021

Kaplan D. E., Krnjaic G. Z., Rehmann K. R., Wells C. M., 2011, *J. Cosmol. Astropart. Phys.*, 1110, 011

Kaplinghat M., Tulin S., Yu H.-B., 2016, *Phys. Rev. Lett.*, 116, 041302

Kauffmann G., White S. D. M., Guiderdoni B., 1993, *MNRAS*, 264, 201

Kennedy R., Frenk C., Cole S., Benson A., 2014, *MNRAS*, 442, 2487

Kim T.-S., Viel M., Haehnelt M. G., Carswell R. F., Cristiani S., 2004, *MNRAS*, 347, 355

Kim S. Y., Peter A. H. G., Hargis J. R., 2017, *Phys. Rev. Lett.*, 121, 211302

Klypin A., Kravtsov A. V., Valenzuela O., Prada F., 1999, *ApJ*, 522, 82

Kobayashi T., Murgia R., De Simone A., Iršič V., Viel M., 2017, *Phys. Rev. D*, 96, 123514

Kulkarni G., Hennawi J. F., Oñorbe J., Rorai A., Springel V., 2015, *ApJ*, 812, 30

Lee S. K., Lisanti M., Safdi B. R., Slatyer T. R., Xue W., 2016, *Phys. Rev. Lett.*, 116, 051103

Lovell M. R. et al., 2012, *MNRAS*, 420, 2318

Lovell M. R., Frenk C. S., Eke V. R., Jenkins A., Gao L., Theuns T., 2014, *MNRAS*, 439, 300

Lovell M. R. et al., 2018, *MNRAS*, 477, 2886

Macciò A. V., Fontanot F., 2010, *MNRAS*, 404, L16

Macias O., Gordon C., Crocker R. M., Coleman B., Paterson D., Horiuchi S., Pohl M., 2018, *Nat. Astron.*, 2, 387

Marinacci F. et al., 2018, *MNRAS*, 480, 5113

McDonald P., Miralda-Escudé J., Rauch M., Sargent W. L. W., Barlow T. A., Cen R., Ostriker J. P., 2000, *ApJ*, 543, 1

Moore B., Ghigna S., Governato F., Lake G., Quinn T., Stadel J., Tozzi P., 1999, *ApJ*, 524, L19

Murgia R., Merle A., Viel M., Totzauer M., Schneider A., 2017, *J. Cosmol. Astropart. Phys.*, 1711, 046

Murgia R., Iršič V., Viel M., 2018, *Phys. Rev. D*, 98, 083540

Naiman J. P. et al., 2018, *MNRAS*, 477, 1206

Nasir F., Bolton J. S., Becker G. D., 2016, *MNRAS*, 463, 2335

Nelson D. et al., 2018, *MNRAS*, 477, 450

Nori M., Murgia R., Iršič V., Baldi M., Viel M., 2019, *MNRAS*, 482, 3227

Oñorbe J., Hennawi J. F., Lukic Z., Walther M., 2017, *ApJ*, 847, 63

Palanque-Delabrouille N. et al., 2013, *A&A*, 559, A85

Pawlowski M. S. et al., 2014, *MNRAS*, 442, 2362

Peeples M. S., Weinberg D. H., Davé R., Fardal M. A., Katz N., 2010, *MNRAS*, 404, 1281

Pillepich A. et al., 2018a, *MNRAS*, 473, 4077

Pillepich A. et al., 2018b, *MNRAS*, 475, 648

Planck Collaboration XIII, 2016, *A&A*, 594, A13

Pontzen A., Governato F., 2014, *Nature*, 506, 171

Rauch M. et al., 1997, *ApJ*, 489, 7

Read J. I., Iorio G., Agertz O., Fraternali F., 2017, *MNRAS*, 467, 2019

Robertson A. et al., 2018, *MNRAS*, 476, L20

Rocha M., Peter A. H. G., Bullock J. S., Kaplinghat M., Garrison-Kimmel S., Oñorbe J., Moustakas L. A., 2013, *MNRAS*, 430, 81

Rorai A., Hennawi J. F., White M., 2013, *ApJ*, 775, 81

Sameie O., Creasey P., Yu H.-B., Sales L. V., Vogelsberger M., Zavala J., 2018, *MNRAS*, 479, 359

Sawala T. et al., 2016, *MNRAS*, 457, 1931

Schaye J. et al., 2015, *MNRAS*, 446, 521

Schewtschenko J. A., Wilkinson R. J., Baugh C. M., Böhm C., Pascoli S., 2015, *MNRAS*, 449, 3587

Schneider A., Smith R. E., Macciò A. V., Moore B., 2012, *MNRAS*, 424, 684

Seljak U., Makarov A., McDonald P., Trac H., 2006, *Phys. Rev. Lett.*, 97, 191303

Silk J., 1968, *ApJ*, 151, 459

Sokolenco A., Bondarenko K., Brinckmann T., Zavala J., Vogelsberger M., Bringmann T., Boyarsky A., 2018, *J. Cosmol. Astropart. Phys.*, 12, 038

Spergel D. N., Steinhardt P. J., 2000, *Phys. Rev. Lett.*, 84, 3760

Spergel D. N. et al., 2003, *ApJS*, 148, 175

Springel V., 2010, *MNRAS*, 401, 791

Springel V. et al., 2018, *MNRAS*, 475, 676

Theuns T., Leonard A., Efstathiou G., Pearce F. R., Thomas P. A., 1998, *MNRAS*, 301, 478

van den Aarssen L. G., Bringmann T., Pfrommer C., 2012, *Phys. Rev. Lett.*, 109, 231301

Viel M., Lesgourges J., Haehnelt M. G., Matarrese S., Riotto A., 2005, *Phys. Rev. D*, 71, 063534

Viel M., Becker G. D., Bolton J. S., Haehnelt M. G., 2013, *Phys. Rev. D*, 88, 043502

Vogelsberger M., Zavala J., Loeb A., 2012, *MNRAS*, 423, 3740

Vogelsberger M., Genel S., Sijacki D., Torrey P., Springel V., Hernquist L., 2013, *MNRAS*, 436, 3031

Vogelsberger M. et al., 2014a, *MNRAS*, 444, 1518

Vogelsberger M., Zavala J., Simpson C., Jenkins A., 2014b, *MNRAS*, 444, 3684

Vogelsberger M. et al., 2014c, *Nature*, 509, 177

Vogelsberger M., Zavala J., Cyr-Racine F.-Y., Pfrommer C., Bringmann T., Sigurdson K., 2016, *MNRAS*, 460, 1399

Vogelsberger M., Zavala J., Schutz K., Slatyer T. R., 2019, *MNRAS*, 484, 5437

Walther M., Hennawi J. F., Hiss H., Oñorbe J., Lee K.-G., Rorai A., O'Meara J., 2018, *ApJ*, 852, 22  
 Wang J., White S. D. M., 2007, *MNRAS*, 380, 93  
 Weinberger R. et al., 2017, *MNRAS*, 465, 3291  
 Weinberg D. H., Hernquist L., Katz N., Croft R., Miralda-Escudé J., 1997, in Petitjean P., Charlot S., eds, Proc. 13th IAP Astrophysics Colloquium, Structure and Evolution of the Intergalactic Medium from QSO Absorption Line System. Institut d'Astrophysique, Paris, p. 133  
 Yoshida N., Springel V., White S. D. M., Tormen G., 2000, *ApJ*, 544, L87  
 Zaldarriaga M., Hui L., Tegmark M., 2001, *ApJ*, 557, 519  
 Zavala J., Jing Y. P., Faltenbacher A., Yepes G., Hoffman Y., Gottlöber S., Catinella B., 2009, *ApJ*, 700, 1779  
 Zavala J., Vogelsberger M., Walker M. G., 2013, *MNRAS*, 431, L20  
 Zehavi I. et al., 2011, *ApJ*, 736, 59

## APPENDIX A: RESOLUTION TESTS

In Fig. A1, we compare the  $z = 5$  halo mass functions measured in the sDAO high-resolution (HR,  $20 h^{-1}$  Mpc,  $N_p = 2 \times 512^3$ ) and sDAO low-resolution (LR,  $40 h^{-1}$  Mpc,  $N_p = 2 \times 512^3$ ) simulations. The mass functions are converged over the expected range. The LR simulation shows an excess at the very massive end, as these rare haloes are more likely to be found in the larger volume of the LR simulation. It is interesting to note, however, that neither simulation shows an upturn towards the low-mass end, which is usually the characteristic signature of artificial halo formation in WDM simulations. This problem is exacerbated at low resolution – the scale below which these fragments start to dominate scales with the number of particles roughly as  $N_p^{1/3}$  (Wang & White 2007). While this scale is clearly present in the 1.6 keV WDM simulation

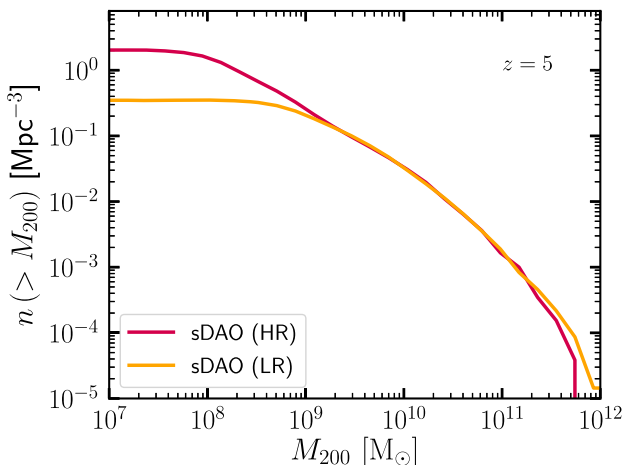


**Figure A1.** Comparison of the cumulative halo mass functions at  $z = 5$  in the sDAO LR ( $40 h^{-1}$  Mpc,  $N_p = 2 \times 512^3$ ) and HR ( $20 h^{-1}$  Mpc,  $N_p = 2 \times 512^3$ ) simulations. The excess at the high-mass end in the LR simulation is due to the larger box size; similarly, the lack of low-mass haloes is due to the lower resolution than in the HR version. Note that the characteristic upturn due to spurious fragmentation, which is clearly visible in WDM models (Wang & White 2007), is no longer clear in the sDAO model at either resolution.

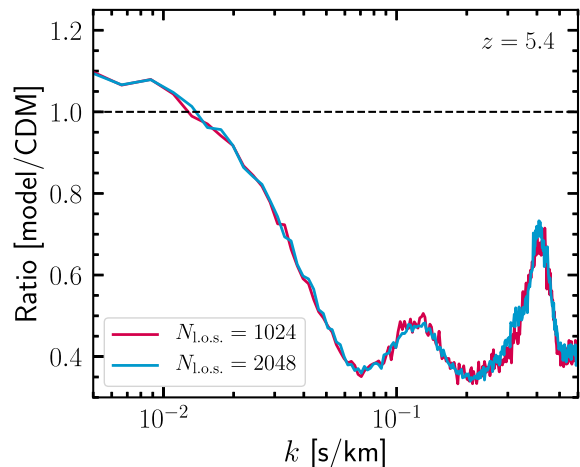


**Figure A2.** Demonstrating the convergence of the 1D Lyman- $\alpha$  flux spectrum ratio with respect to the number of lines of sight chosen for the analysis.

(see Fig. 9), the effect is largely suppressed in the sDAO model at both LR and HR. The reason for this is that while the cut-off in WDM continues indefinitely, the DAO adds power on scales smaller than the initial cut-off, thereby largely offsetting the instability through discreteness effects that are typical of WDM-like simulations.

Fig. A2 justifies our use of 1024 lines of sight for generating mock absorption spectra from our simulations. In this figure we show the ratio (sDAO/CDM) of the 1D flux power spectrum at  $z = 5.4$  using 1024 (red) and 2048 (blue) lines of sight. The two curves show excellent convergence across all scales. We have checked explicitly that individual power spectra (rather than simply the ratio) are converged as well. We find that, in general, the truncated Gaussian smoothing kernel (Altay & Theuns 2013; see also equation 2) is relatively robust to the number of skewers used to generate the mock spectra.

## APPENDIX B: DARK MATTER MODEL PARAMETERS

We list in Table B1 the atomic DM parameters used to generate our sDAO model. For more details on the model, see Cyr-Racine & Sigurdson (2013).

**Table B1.** Atomic DM particle parameters used to generate our sDAO model.  $T_{\text{DR}}$  is the temperature of the dark radiation bath, while  $T_{\text{CMB}}$  is the cosmic microwave background temperature.

Parameter	Description	Value
$\xi$	$T_{\text{DR}}/T_{\text{CMB}}$	0.15
$\alpha_D$	The dark fine structure constant	0.02
$B_D$	The dark atom binding energy	1.7 keV
$m_{\text{DM}}$	The dark atom mass	500 MeV

This paper has been typeset from a  $\text{\TeX}/\text{\LaTeX}$  file prepared by the author.